Research Square

Preprints are preliminary reports that have not undergone peer review. They should not be considered conclusive, used to inform clinical practice, or referenced by the media as validated information.

A lipidome landscape of aging in mice

Hiroshi Tsugawa

htsugawa@go.tuat.ac.jp

RIKEN Center for Sustainable Resource Science https://orcid.org/0000-0002-2015-3958

Tomoaki Ishihara

RIKEN

Kota Ogasa

Keio University

Seigo Iwanami

Keio University

Aya Hori

RIKEN

Mikiko Takahashi

RIKEN

Yutaka Yamada

RIKEN

Aki Minoda

RIKEN

Makoto Arita

RIKEN Center for Integrative Medical Sciences https://orcid.org/0000-0001-9902-0463

Biological Sciences - Article

Keywords: lipidome, aging, microbiota, sex, metabolism, multi-omics

Posted Date: October 26th, 2022

DOI: https://doi.org/10.21203/rs.3.rs-2139359/v1

License: This work is licensed under a Creative Commons Attribution 4.0 International License. Read Full License

Additional Declarations: There is **NO** Competing Interest.

Version of Record: A version of this preprint was published at Nature Aging on April 12th, 2024. See the published version at https://doi.org/10.1038/s43587-024-00610-6.

Abstract

Understanding the molecular mechanisms associated with aging is important to improve the longevity of healthy individuals. Herein, we performed untargeted lipidomics to elucidate the relationship between aging and lipid metabolism in 13 mouse tissues at various life stages (2, 12, 19, and 24 months), in which sex and microbiome dependencies (specific pathogen free/germ free) were investigated. By analyzing 2,817 unique molecular profile data of 121 lipid subclasses, we characterized the common and tissue-specific lipidome changes associated with aging. For example, bis(monoacylglycerol)phosphate containing polyunsaturated fatty acids was enriched in various organs during aging, while other phospholipids containing saturated and monounsaturated fatty acids were decreased. In addition, we discovered an age-dependent increase of sulfonolipid (SL), which is biosynthesized in Alistipes and Odoribacter genera. SL molecules were absent in germ-free mice. Furthermore, the molecules appeared to be translocated from the intestinal lumen to various tissues such as the liver, kidney, and spleen. In the kidney, the associations of glycolipids such as galactosyl ceramides (GalCer), galabinosyl ceramides (Gal2Cer), trihexosyl ceramides (Hex3Cer), and mono and digalactosyl diacylglycerols were found in male mice, in which two lipid classes Gal2Cer and Hex3Cer were significantly enriched in aged mice. Integrated analysis of the kidney transcriptome revealed uridine diphosphate galactosyltransferase UGT8a, alkylglycerone phosphate synthase, and fatty acyl-CoA reductase 1 as potential enzymes responsible for male-specific glycolipid biosynthesis in vivo, which would be relevant to sex dependency in kidney diseases. Our lipidome results will become an important resource, led to the understanding of the molecular mechanisms underlying cellular senescence and age-related diseases.

Introduction

Lipids are diverse and multifunctional in living organisms and serve as signaling molecules, energy storage molecules, and cellular membranes[1]. These functions involve thousands of lipid species in mammalian cells, and the dysregulation of lipid metabolism is associated with various diseases such as atherosclerosis[2], cancer[3], non-alcoholic steatohepatitis[4], and chronic kidney disease[5]. Undoubtedly, the risk of chronic diseases is related to aging processes, and the understanding of changes in lipid metabolism is likely to illuminate the biological mechanisms associated with aging[6-9].

To date, the potential link between aging and lipid metabolism has been studied. For example, an increased activity of sphingomyelinase that convert sphingomyelin to ceramide results in accumulation of ceramides in the elderly patients in a human cohort study[10]. Additionally, low serum ceramide levels are associated with a reduced risk of dementia and Alzheimer's disease in elderly women[11]. The biosynthetic pathway and regulation of neutral lipids are also linked to longevity. Deficiency of diacylglyceride acyltransferase 1 improves longevity and leanness in female mice, where age-onset obesity and inflammation in white adipose tissue are protected[12]. Furthermore, the ratio of saturated fatty acids (SFA), monounsaturated fatty acids (MUFA), and polyunsaturated fatty acids (PUFA) is associated with the susceptibility of the cellular membrane to peroxidation. The accumulation of reactive oxygen

species during aging leads to lipid peroxidation, which damages cellular membrane components[13]. Nevertheless, the relationship between fatty acid properties and longevity is tissue-specific, sex-linked, and species dependent. For example, lipidomic studies investigating human erythrocyte and lymphocyte membranes showed that centenarians have more PUFAs than that of the other aged group[14,15], while the concentration of phospholipids containing docosahexaenoic acid in longest-living rodents (naked mole-rats) is lower than that of mice[16]. In addition, recent studies have shown an association between aging and microbiota, in which lipid metabolism is highly affected by the composition of the microbiome and food intake conditions[17-21]. These results strongly indicate the importance of understanding the metabolic changes in diverse lipid molecules in various mammalian tissues under sex- and microbiota-dependent conditions.

Untargeted lipidomics has great potential to reveal the diversity of lipidomes, covering approximately 1000 lipid molecules per single specimen[22,23]. Although an untargeted approach results in higher false positive annotations compared to the targeted approach, the false discovery rate (FDR) can now be well controlled using current state-of-the-art computational mass spectrometry techniques[23]. Therefore, we applied untargeted lipidomics using liquid chromatography coupled with tandem mass spectrometry (LC-MS/MS) to elucidate the changes in lipidomes in tissues during aging (**Fig. 1a**). Thirteen biological samples (kidney, liver, lung, spleen, muscle, bone marrow, plasma, skin from ear, skin from back, mesentery, small intestine, large intestine, and feces) were examined in this study. The lipidome was investigated in males and females of different ages (2, 12, 19, and 24 months) in the presence (specific pathogen-free; SPF) or absence of microbiota (germ-free; GF). Although there are several studies that have applied a lipidomic technique to specific tissues[24-29] (e.g., a study encompassing the metabolome atlas of brain tissue during aging[30]), the current study is the first to comprehensively investigate the lipidome of multiple organs with differences in sex and the microbiome. Furthermore, a multi-omics approach using transcriptome and lipidome data was used to reveal the relationship between gene expression and the lipid profile of the kidney.

The significance of our study is that it offers comprehensive lipidomic changes associated with aging in mice from four different backgrounds: male and SPF (male/SPF), male and GF (male/GF), female and SPF (female/SPF), and female and GF (female/GF). Furthermore, to examine the details of the mouse lipidome, we updated our software program MS-DIAL 4[23], which is a MS data processing environment in which 17 lipid subclasses containing several gangliosides, sterols, and glycolipids were newly introduced into the lipid annotation platform, covering 136 lipid subclasses that contain microbiota- and tissue-specific lipid molecules. We used the platform of untargeted lipidomics to reveal that certain common lipid changes are not affected by male/female and SPF/GF differences, e.g., accumulation of PUFA containing complex lipids, such as bis(monoacylglycerol)phosphate (BMP). Moreover, we discovered that the microbiota-derived sulfonolipid (SL) was associated with aging and that the molecule appeared to be translocated to various organs, while most of the microbiota lipids were only detected in the fecal matter. Furthermore, male-specific accumulation of glycolipids, including galactosyl ceramide (GalCer) and monogalactosyldiacylglycerol (MGDG), was observed in the kidney, and a uridine

diphosphate (UDP) galactosyltransferase, UGT8a, was considered responsible for the metabolic regulation.

Materials And Methods

Mouse experiment

All animal experiments were performed in accordance with the ethical protocol approved by the RIKEN Center for Integrative Medical Sciences (2019-015(2)). Four-week-old male and female C57BL/6N mice were purchased from CLEA (Tokyo, Japan). The GF mice were housed in GF isolators at the animal facility at RIKEN. All the mice were fed the chow of AIN-93M (CLEA Japan, Tokyo, Japan). The kidney, liver, lung, spleen, skeletal muscle, bone marrow, plasma, ear skin, back skin, mesentery, small intestine, large intestine, and feces were harvested. Tissues were frozen immediately after dissection and stored at −80°C until lipid extraction. The details of the time-course experiments are described in **Supplementary Table 1**.

Lipid extraction

Lipid extraction was performed according to a previously reported method, in which a mixed solvent containing methanol, chloroform, and water ($MeOH:CHCl_3:H_2O$, 1:2:0.2, v/v/v) was utilized. Details of the solvent volumes and internal standards used in this study are described in **Supplementary Tables 2 and 3**. Briefly, the tissues were homogenized using a multi-bead shocker (YASUI KIKAI, Japan) with a metal cone (YASUI KIKAI, Japan) at 2500 rpm for 15 s × 2, and MeOH was added to the homogenate according to the tissue weight. After the solvent was homogenized again at 2000 rpm for 10 s, the appropriate amount of MeOH (<100 μL) solving 1–5 mg tissue weight was transferred to a 2-mL glass tube. After the solvent was added to 175 μL of MeOH, 25 μL of MeOH containing internal standards was added to the solvent, and the mixture was sonicated for 2 min. For bone marrow cells and plasma samples, 175 μL of MeOH containing 10^6 cells and 20 μL, respectively, were prepared without the homogenization process. After the solvent was incubated for 2 h on ice, 100 μL of chloroform was added, and the mixture was sonicated for 2 min. After the solvent was incubated for 1 h at room temperature (set to 20°C), 20 μL of Milli-Q water was added, and the mixture was vortexed for 10 s. After 10 min of incubation at room temperature, the solvent was centrifuged at 2000×g for 10 min at 20°C, and the supernatant was transferred to an LC-MS vial (Agilent Technologies).

Reverse phase liquid chromatography tandem mass spectrometry

The experimental details are described in a previous study[31]. Briefly, the LC system consisted of a Waters Acquity UPLC system. Lipids were separated on an Acquity UPLC Peptide BEH C18 column (50 × 2.1 mm;

1.7 μm) (Waters, Milford, MA, USA). The column was maintained at 45°C and a flow rate of 0.3 mL/min. The mobile phases consisted of (A) 1:1:3 (v/v/v) acetonitrile (ACN):MeOH:water with ammonium acetate (5 mM) and 10 nM ethylenediaminetetraacetic acid (EDTA) and (B) 100% isopropanol with ammonium acetate (5 mM) and 10 nM EDTA. A sample volume of 0.5–3 μL, according to the biological samples, was used for the injection, and the volume was optimized so that the highest peak of lipids was less than the upper detection limit of the MS. The separation was conducted under the following gradient: 0 min 0% (B), 1 min 0% (B), 5 min 40% (B), 7.5 min 64% (B), 12 min 64% (B), 12.5 min 82.5% (B), 19 min 85% (B), 20 min 95% (B), 20.1 min 0% (B), and 25 min 0% (B). The temperature of the samples was maintained at 4°C.

The MS detection of lipids was performed using a quadrupole/time-of-flight MS (TripleTOF 6600; SCIEX, Framingham, MA, USA). All analyses were performed in high-resolution mode in MS1 (~35,000 full width at half maximum (FWHM)) at high sensitivity mode (~20,000 FWHM) in the MS2. Data-dependent MS/MS acquisition was performed. The parameters were as follows: MS1 and MS2 mass ranges, *m/z* 70–1250; MS1 accumulation time, 200 ms; MS2 accumulation time, 70 ms; collision energy, +40/−42 eV; collision energy spread, 15 eV. Mass calibration was automatically performed using an APCI-positive/negative calibration solution via a calibration delivery system. All other parameters have been described in a previous report[31].

Hydrophilic interaction chromatography (HILIC) phase liquid chromatography tandem mass spectrometry

The DCpak P4VP column (150 × 2.1 mm; 3.0 μm) (DAICEL, Japan) was used. The column was maintained at 40°C and a flow-rate of 0.2 mL/min. The mobile phases consisted of (A) 95:5 (v/v) MeOH:water with ammonium acetate (10 mM) and 0.2% acetic acid and (B) 95:2:3 (v/v/v) ACN:MeOH:water with ammonium acetate (10 mM) and 0.2% acetic acid. A sample volume of 2 μL of kidney lipid extract was used for injection. Separation was conducted under the following gradient: 0 min 100% (B), 30 min 0% (B), 31 min 0% (B), 31.1 min 100% (B), and 40 min 100% (B). The other LC-MS parameters were the same as those used for reverse-phase LC-MS analysis. The temperature of the samples was maintained at 4°C. C17 galabiosyl ceramide, C17 lactosyl (β) ceramide, C18 galactosyl (β) ceramide, and C18 glucosyl (β) ceramide were purchased from Avanti Polar Lipids and used to confirm RTs.

MS-DIAL analysis

The *in silico* reference spectra of 17 lipid subclasses were created according to a previously described method[23]. The MS/MS spectra of gangliosides were experimentally confirmed by analyzing authentic standard compounds. For the other lipid subclasses, MS/MS spectra were obtained from the literature (**Supplementary Table 4**). A decision tree (rule-based) algorithm considering the existence of diagnostic

fragment ions for lipid annotation was implemented. The expected RTs were predicted using our XGBoost-based machine learning methodology, which has been described in a previous report[23]. The summary of fragment ion annotations is also available at our website (http://prime.psc.riken.jp/compms/msdial/lipidnomenclature.html).

The version 4.20 algorithm of MS-DIAL was utilized for the analysis. The data processing parameters for minimum amplitude (for peak picking) and RT tolerance (for lipid annotation and peak alignment) were set to 500, 2.0 min, and 0.1 min, respectively. Other parameters are listed in **Supplementary Table 5**. RT filtering for lipid annotation was not utilized for HILIC lipidomics data. The annotated results were curated manually. The representative adduct forms used for lipid quantification are shown in **Supplementary Table 6**. The lipid molecules were semi-quantified using internal standards according to a previously described method: the value of lipid quantification was provided in pmol/mg tissue, pmol/μL plasma, or pmol/10^6 cells. Pairs of lipid subclasses and internal standards are described in **Supplementary Table 6**. The lipidome results are available in **Supplementary Data 1**.

Transcriptome analysis

Tissue samples were homogenized in 700 μL of TRIzol reagent (Thermo Fisher Scientific, USA) per 50 mg of tissue in a glass tube. The supernatant was collected after centrifugation of the cell lysate for 10 min at 12000 × g at 4°C. After adding 100 μL of chloroform to 500 μL of the supernatant, the mixture was incubated for 3 min at room temperature (set to 22°C) and centrifuged for 15 min at 12000 × g at 4°C. Then, 120 μL of 70% ethanol (w/w) was added to 120 μL of the supernatant and suspended. Total RNAs was extracted from the mixture using the RNeasy Plus Mini Kit (Qiagen, Hilden, Germany), according to the manufacturer's protocol. Quality checks were performed using a bioanalyzer (Agilent Technologies, USA) in accordance with the Agilent RNA 6000 Nano Assay protocol. RNA integrity number of the samples was confirmed to be 6.9–9.1 (with an average of 8.6). Subsequently, the library was synthesized using the NEB Next Ultra RNA Library Prep Kit for next-generation sequencing. The pooled libraries were sequenced on an Illumina HiSeq 2500, and 50 bp single-end reads were generated. The reads were aligned using STAR software onto a transcript reference based on UCSC_mm10 (mouse reference). After the genes in which the minimum value of read count is less than 10 or the gene name contains "rik" were excluded, differentially expressed genes were calculated using the R/Bioconductor package, DESeq2 (1.28.1). The transcriptome data is available in **Supplementary Data 2**.

Statistical analysis

Statistical analysis and data visualization were performed using the R language environment (version 4.1.2).

Results

The optimal amounts of plasma (~20 μL), cells (~10^6 cells), and tissues (~5 mg) were subjected to lipid extraction followed by LC-MS/MS analysis (**Fig. 1b**). Lipid annotation in MS-DIAL was performed using the MS/MS characterization system of lipids and 2.0 min RT tolerance to the predicted RT database. The annotation results were manually curated. After the peak alignment was performed by the RT tolerance of 0.1 min and *m/z* tolerance of 0.015 Da, the semi-quantification values were calculated by the internal standards (see **Materials and Methods**). The molecules in plasma (408) and kidney (~ 961) were characterized per biospecimen. In total, 2,817 unique molecules from 121 lipid subclasses were annotated and used for data interpretation.

Principal component analysis (PCA) using auto-scaled values was performed to examine the major variances of the lipidomic datasets (**Figure 2**). Individuals of each group were mapped at a topology similar to that of the PCA score plots, indicating that our lipidomics output obtained from a long experimental procedure from mouse bleeding to MS data analysis is valuable for further statistical analyses. We observed that the largest variances, i.e., at the first PC (PC1), in the kidney and feces reflected the sex and microbiome backgrounds, respectively. The results of the fecal lipidome changes indicated that many lipid molecules are biosynthesized and/or degraded by intestinal microbiota. However, the SPF and GF differences were not reflected significantly in PCA by the host lipidomes in the small and large intestines. Furthermore, the plasma lipidome of young GF mice was clearly distinguished from the others, in which triglycerides (TG) were enriched in young GF mice according to the loading values (**Supplementary Figure 1**). A previous study investigating serum, liver, and adipose tissue of young mice (aged 12–14 weeks) reported that the serum TG level was lower in SPF mice than in GF mice, while the TG lipids were increased in the liver and adipose tissue of SPF mice[32]. Our results are consistent with the previous observations (**Figure 3**). Moreover, sex-specific lipidome differences were clearly observed in the kidneys at PC1. In addition, age-dependent lipid changes were reflected in the PCA score plots of several tissues, such as the kidney, liver, mesentery, plasma, bone marrow, and skin. We also observed a larger individual difference in aged mice (1.5–2 years old mice), indicating that many biological and environmental factors accumulate during aging.

In contrast to unsupervised mathematical analysis such as PCA, the supervised chemometrics approach is useful for extracting lipidome changes with aging. We applied orthogonal partial least squares regression (OPLS-R) to investigate lipid changes during aging (**Figure 3**). Importantly, we used the entire lipidome data, which contained four different backgrounds (SPF/male, GF/male, SPF/female, and GF/female) as the variables for OPLS-R. The Q^2 values calculated by 6-fold cross validations indicated that the prediction of age states is possible using the information of the lipid metabolome. Among the tissues examined, the Q^2 values in the kidney, lung, mesentery, muscle, spleen, ear skin, and large intestine exceeded 0.70, indicating that a large proportion of lipids was associated with aging in these organs. Of these, the highest Q^2 value was observed in the kidneys. We investigated the variable importance for prediction (VIP) values, which indicate the important metabolites used for OPLS-R model

creation. The top 10 VIPs, whose chromatogram peak shape of metabolites was of good quality (for quantification), were used for the interpretation of lipid changes. Decreases in phosphatidylcholine (PC), phosphatidylethanolamine (PE), phosphatidylserine (PS), phosphatidylinositol (PI), diacylglycerol (DG), and TG containing SFA and MUFA were observed in the lungs, mesentery, muscle, ear skin, large intestine, and plasma. In contrast, these lipid classes containing PUFAs, particularly 20:4 and 22:6, were increased in the liver, lung, muscle, bone marrow, and small intestine. An increase in the PUFA/MUFA ratio during aging has been reported in human and *Caenorhabditis elegans*[9], indicating that our aging-lipidomics study investigated the changes in lipids that have previously been unknown. BMP-containing PUFAs clearly increased with aging in the kidney, liver, muscle, spleen, and small intestine. Because BMP lipids are enriched in the late endosome and lysosome and promote acidic sphingomyelinase activity, the BMP lipid signature may explain the accumulation of ceramides during aging in mammalian organisms[33,34]. Increases in cholesteryl esters (CE) have also been observed in several tissues, such as the kidney, lung, spleen, and large intestine. Furthermore, decrease in ceramides, epidermal acyl ceramides, SHexCer (sulfatide), gangliosides (NGcGM3, GD3), and cardiolipin (CL) were observed, which may be linked to the functional defect of cell organelles such as mitochondria, endoplasmic reticulum, Golgi body, and endosome systems. Importantly, these common or tissue-specific lipid changes can be considered as common metabolic signatures associated with aging because the OPLS-R model was constructed using the entire lipidome data that contained all mice groups examined in this study.

We next explored age-dependent lipid changes influenced by sex and the gut microbiota (**Fig. 4a**). The quantitative value of each lipid subclass was calculated by summing the quantitative values of molecules annotated by the same lipid subclasses. The fecal lipidome indicated that the profiles of many lipid subclasses were affected by the gut microbiota, and the orange circle indicates that the lipid subclass was enriched in SPF mice compared to GF mice. Greater than four-fold increases in unconjugated bile acid (BA); acyl diacylglyceryl glucuronide (ADGGA); several ceramide subtypes (Cer_ADS, Cer_AP, Cer_BDS, and Cer_EBDS); glycolipids such as MGDG, digalactosyl DG (DGDG), and NGcGM3; fatty acid esters of hydroxy fatty acid (FAHFA), PE and phosphatidylglycerol (PG), ceramide PE and PI (PE_Cer and PI_Cer); SL; and *N*-acyl glycine, glycylserine, and ornithine (NAGly, NAGlySer, NAOrn) were observed in SPF mice than in GF mice. In contrast, glycine- and taurine-conjugated BAs were substantially elevated in GF mice owing to the absence of intestinal bacteria responsible for BA deconjugation. We also observed sex-specific lipid profiles in several lipid subclasses, such as TG, lyso-PG, and glycolipids in the fecal lipidome. Interestingly, sex specificity in lipid metabolites was substantially observed in the kidney, where the glycolipids containing dihexosyl Cer (Hex2Cer), trihexosyl Cer (Hex3Cer), MGDG, DGDG, and the alkylacyl types (Ether MGDG and Ether DGDG) were enriched in male mice, and the percentage, i.e., the value of male/(male + female) was >80%. Furthermore, Hex2Cer and Hex3Cer levels in the kidney increased with aging. The major acyl chain properties of these glycosylceramides were 18:1;O2/16:0, 18:2;O2/16:0, 18:1;O2/24:0, and 18:2;O2/24:0, where the sphingobase moiety is considered sphingosine (18:1(4E);1OH,3OH) and sphingadienine (18:2(4E,14Z);1OH,3OH) according to a previous study[35]. Interestingly, MGDG and DGDG molecules, known as plant thylakoid membrane lipids, were detected in the kidney. Although such

glycosyldiacylglycerols are ubiquitous as a minor component of the brain and other nervous tissues[36,37] and are enriched in oligodendrocytes, our results indicated that both diacyl- and alkylacyl-type glycosyldiacylglycerols were present in the kidney, and the molecules were enriched in male mice and not affected by the gut microbiome. Furthermore, we found that SLs, known as microbiota-derived lipids, were detected in peripheral tissues, whereas most of other microbiota-derived lipids were not detected (**Fig. 4b and 4c**). The major component of SL was SL 17:0/17:0;O in peripheral tissues, which increased with aging. Two bacterial genera, *Alistipes* and *Odoribacter*, are producers of SL. Several bioactivities of SL have been reported, including antagonistic action on von Willebrand factor receptors, cytotoxicity in cancer cells, inhibition of DNA polymerase, and anti-inflammatory effect[38]. Overall, our aging lipidome atlas clearly demonstrates lipid diversity and its unique profiles during aging. Of these, we believe that it is important to investigate the mechanism of kidney lipidome changes, because the kidney lipidome showed a characteristic profile depending on sex, the presence of intestinal bacteria, and a strong age-dependent variation.

We performed RNA-seq analysis of the kidney tissue of the same mice used for lipidome profiling. According to the PCA score plot, male and female transcriptome data were separated by PC1 with a contribution ratio of 57.3% (**Fig. 5a**). This result indicates that kidney gene expression is highly affected by sex, as supported by previous studies[39,40]. Similar tendency was observed in the volcano plot of male and female comparisons where 601 and 1,102 genes were up and downregulated, respectively, with the condition of >0.5 $\log_2$ fold change and <0.05 adjusted *p*-value (**Fig. 5b**). Contrastingly, only 18 and one gene were recognized as up and downregulated genes, respectively, between SPF and GF groups, indicating less effect of microbiome on the transcriptome in the kidney. Between aged (24 months) and young (two months) mice, we detected 32 upregulated and 100 downregulated genes. Previous studies have reported that aldehyde dehydrogenase 1 family member A1 (ALDH1A1), a key enzyme of retinoid metabolism, is one of the most prominently upregulated proteins and genes in aged kidney[41]. This result suggests that our kidney transcriptome data are comparable to those in previous literature and will provide useful information for subsequent data interpretation using sex, aging, and microbiota-dependent transcriptome profiles.

Gene ontology (GO) analysis using the significant genes described above was performed by g:Profiler[42], which provided the GO terms of molecular function, biological process, and cellular component, in addition to the pathway enrichments in the KEGG and Reactome databases (**Fig. 5c**). According to the top five enriched ontology terms for each source, we observed the enrichment of terms related to stress and immune responses in aged mice owing to the significant increase in gene expression, including vascular cell adhesion molecule 1, a chaperone protein resistance to inhibitors of cholinesterase 3, poly(ADP-ribose) polymerase family member 3, solute carrier family 11 member 1, tumor necrosis factor receptor superfamily member 1 B, phosphatidylinositol-4,5-bisphosphate 3-kinase catalytic subunit delta, and ALDHs (see **Source data**). Moreover, we observed many terms related to “metabolism” including lipid-related metabolisms when upregulated genes in male mice were applied to g:Profiler application. The genes included many of UDP glycosyltransferases (UGTs), cytochrome P450s (CYPs), acyl-coenzyme A

(CoA) oxidases, peroxisomal trans-2-enoyl-CoA reductase, phytanoyl-CoA 2-hydroxylase, ALDHs, etc. In contrast, the terms related to the kidney's main functions, including the renin-angiotensin system, drug metabolism, and regulated calcium reabsorption, were enriched in female mice. They include glutathione S-transferases, the kallikrein gene family, and serine proteases for proteins related to blood pressure reduction. The severity of acute and chronic kidney injury is generally higher in males and lower in females[43], and these differences in gene expression may contribute to the phenotypic differences in the kidney.

Furthermore, we investigated the transcription factors (TFs) and histone modifications (HMs) that would regulate the significant changes in males versus females and in aged versus young mice using ChIP-Atlas[44] (**Fig. 5d**). Interestingly, signal transducer and activator of transcription 3 (STAT3), vitamin D receptor (VDR), androgen receptor (AR), and hepatocyte nuclear factor 4-alpha (HNF4a) were commonly detected as significant TFs between males and females and between aged and young mice. HNF4a is the main TF for drug-metabolizing enzymes in the kidney[45] and regulates peroxisome proliferator-activated receptor (PPAR)-α and γ, which are highly associated with lipid metabolism[46]. Sex differences in renal metabolism are mediated by testosterone, involving AR-dependent signaling pathways in male, but not female, kidneys[47]. In addition, STAT3 activity increases with age in epithelial compartments of the renal cortex[48]. Furthermore, the AR N-terminal domain is activated by the cytokine interleukin 6, which is mediated through the STAT3 signal transduction pathway, and androgen-STAT3 activation might contribute to sex disparity in human simple renal cyst disease[48,49]. In addition, renal vitamin D metabolism is regulated by estradiol and testosterone, and age-dependent dysfunction of vitamin D metabolism, including deficiency of VDR activation, is also related to chronic kidney disease[50,51]. The TF results are further discussed along with the lipid pathway map in the discussion section. Furthermore, the prediction of HMs in the kidney suggested that three major active histone marks, acetylation to the 9th and 27th lysine residues on histone H3 (H3K9ac, H3K27ac) and trimethylation to the 4th lysine residue on histone H3 (H3K4me3), were enriched in male and aged mice, indicating that these HMs may act as regulators of the unique TF profiles of the kidney. However, only three genes (ALDH1a7, CYP2D12, CYP2D13) and two genes (apelin receptor APLNR, NYN domain, and retroviral integrase containing NYNRIN) were commonly upregulated and downregulated in both male and aged mice, respectively (**Fig. 5e**). The results of transcriptome analysis, including TF predictions, indicate that many aging- and sex-associated genetic changes in the kidney are related to lipid metabolism.

Next, we performed an integrated analysis of the transcriptome and lipidome data of the kidney using weighted correlation network analysis (WGCNA)[52] to investigate the associations between gene expression and lipid metabolites during aging (**Fig. 6a**). In total, 16 and 24 clusters were established from lipidome and transcriptome data, respectively. As expected, half of the clusters were significantly associated with aging or sex differences. In contrast, only one lipid cluster (group 11) consisting of SL, bile acids, and phospholipids containing odd carbon chains was associated with the existence of the microbiome. We focused on lipid clusters 1, 4, 5, 8, and 15 located in the same cluster region of the lipid dendrogram, whose groups were highly associated with sex, aging, and gene clusters. The lipid profile

containing 619 molecules was applied to the lipid ontology enrichment analysis using the LION/web application (**Fig. 6b**)[53]. The ontology terms were evaluated by the analysis of variance values in four groups that contained M24/male, M24/female, M2/male, and M2/female SPF mice, where M24 and M2 denote 24-month-old (aged) and 2-month-old (young) mice, respectively. As a result, the terms related to glycolipid metabolism including “simple glc series,” “dihexosylceramides,” and “hexosylceramides” were significantly enriched. Furthermore, terms related to alkylacyl phospholipid metabolism, in addition to steryl esters, were characterized as significant ontologies. Therefore, we performed a pathway analysis of these lipid metabolisms, along with the profiles of related genes.

The lipid metabolism related to glycosyl ceramides was investigated using lipid and transcriptome profiles (**Fig. 7a**). Interestingly, the abundance of HexCer, Hex2Cer, Hex3Cer, and SHexCer was substantially higher in male mice than in female mice, and an age-dependent increase in Hex2Cer and Hex3Cer was observed. In fact, sex-specific differences in Hex2Cer in the kidney have also been highlighted in a reference map of sphingolipids[54]. By exploring the gene expression profiles related to metabolism, we identified UGT8a, an enzyme that converts ceramide to GalCer, as the gene expression was significantly different between male and female mice. These results indicate that sex-dependent UGT8a expression may affect galactosyl ceramide metabolism by providing GalCer, sulfatide, and Gal2Cer in the kidneys with aging. Furthermore, our untargeted lipidomics characterized MGDG, DGDG, and their ether-linked types (ether MGDG and ether DGDG) in the kidney, whose profiles were also affected by sex differences (**Fig. 7b**). Although the enzymes responsible for MGDG and DGDG have not been fully identified in mammalian organisms, the expression profiles of UGT8a and other significantly changed UGT-related genes, such as UGT2b37, UGT2b38, and UGT2b5, offer novel insights for identifying the machinery responsible for glycosyl glycerolipid metabolism in animals (**Fig. 7c**). In fact, two previous studies reported that the overexpression of rat UGT8a in Chinese hamster ovary (CHO) cells increases MGDG lipid levels, which has been confirmed by thin layer chromatography methods[55,56]. Thus, our finding showing an association between UGT8a and MGDG profiles strongly supports the involvement of UGT8a in the biosynthesis of MGDG and other glycoglycerolipids *in vivo*. We also found age-dependent decreases in ether-bond glycerolipids, such as ether DG, ether TG, ether MGDG, ether PC, ether PI, and ether PS, and these metabolites were enriched in males. We identified two genes as candidates for explaining the lipid profiles: alkylglycerone phosphate synthase (AGPS), the enzyme that converts acyl-dihydroxyacetonephosphate (DHAP) to alkyl-DHAP, and fatty acyl-CoA reductase 1 (FAR1), the enzyme responsible for the reduction of fatty acids to fatty alcohols. As our kidney transcriptome data also showed significant changes in genes related to peroxisome metabolism, the changes in peroxisome-related lipid metabolism during aging may contribute to our understanding of the molecular mechanisms of various kidney diseases. An age-dependent increase in CE, but not in free cholesterol (ST 27:1;O), was also observed where there was no sex dependency (**Fig. 7d**).

To examine the stereochemistry of glycosyl HexCer and Hex2Cer, we analyzed the kidney tissue using HILIC (**Fig. 7e**). As expected, galactosyl ceramide was substantially enriched in male mice, whereas the ion abundance of glucosyl ceramide was mostly the same in male and female mice. Interestingly,

Gal2Cer chromatographic peaks were absent in female mice (at least under the limit of detection), and the ion abundance of Gal2Cer was substantially higher than that of lactosylceramide. Although the substrate of globotriaosylceramide (Gb3, described as Hex3Cer) is known as lactosylceramide, this result suggests that the substrate of Hex3Cer in the kidney is likely to be Gal2Cer. Overall, our integrated analysis clearly shows the unique regulatory mechanism of lipid profile, which is associated with sex- and age-dependent differences.

Based on the WGCNA results, only lipid cluster 11 was significantly associated with SPF/GF and aging parameters. The lipid cluster contained molecules that are likely to be microbiota-derived, including sterol sulfates, bile acids, SLs, and PC containing odd chains. Because the lipid cluster was highly associated with gene clusters 8 and 19, we further investigated the association between microbiota-derived lipid molecules and related genes (**Fig. 8**). Most of the lipid molecules contained in the cluster were significantly affected by the SPF/GF parameter; one sterol sulfate (ST 28:1;O;S), two SLs (SL 17:0;O/16:0 and SL 17:0;O/17:0;O), and one PC (PC 17:1_18:2) were recognized as prominent molecules associated with aging. Indoxyl sulfate is a typical urinary toxic metabolite that causes the progression of chronic kidney disease. Intestinal bacteria produce indole from tryptophan, and sulfotransferase 1A1 (SULT1A1) activity adds the sulfate moiety[57]. In contrast, steroid sulfotransferases such as SULT2B1b are responsible for producing cholesterol sulfate, which have various biological activities such as the inhibition of serine proteases (e.g., pancreatic trypsin and chymotrypsin) and PI3K activities[58]. Our results indicate that the production of sterol sulfate is also affected by the microbiome, and microbiota-specific sulfolipids, including SLs, may contribute to homeostasis in the kidney. Furthermore, the genes contained in clusters 8 and 19 were highly associated with lipid metabolism. The association between the lipids in cluster 11 and the genes in clusters 8 and 19 has not yet been reported. In fact, some bile acids, including chenodeoxycholic acid, regulate a variety of metabolic functions by modulating nuclear receptors such as farnesoid X receptor (FXR), whose activation is important for reducing inflammation and oxidative stress in the kidney[59]. The bromodomain genes adjacent to the zinc finger domain, such as 2 B, centrosomal protein 250 kDa (CEP250), integrator complex subunit 1, transmembrane protein 199, microtubule-associated protein, RP/EB family, member 2, adaptor-related protein complex 2 mu 1 subunit, succinate dehydrogenase complex subunit C integral membrane protein 15 kDa, and tyrosyl-DNA phosphodiesterase 2 (TDP2), are predicted to be the target genes of the FXR TF[60]. Moreover, the associations of Midasin AAA ATPase 1, phosphatidylinositol transfer protein membrane associated 2 (PITPNM2), and BAF chromatin remodelling complex subunit 11b (BCL11b) with the microbiome have also been reported[61,62]. The age-dependent changes in PITPNM2, BCL11b, TDP2, and CEP250 were observed. Therefore, our results contribute to the understanding of the mechanism of host-microbiome interactions from the viewpoint of lipidomes.

Discussion

We demonstrated untargeted lipidomics for 13 biological samples, including tissues, cells, and plasma, with aging. These results provide the largest lipidome landscape to investigate metabolic changes

associated with aging from the viewpoint of sex differences and commensal bacterial dependence. The FDR of MS-DIAL-based automatic lipid annotation was 2–3% with a RT filtering of 2.0 min[23]. We manually curated the annotated results by considering the basis of the equivalent carbon number model of lipids, in which the elution behavior of molecules in reverse phase LC depends on the length of acyl chains and the number of double bonds in lipids. In addition, our results highly compensate for recent reports encompassing the mouse brain metabolome changes associated with aging[30].

The results of OPLS-R demonstrated that (1) the ratio of PUFA/MUFA in complex lipids increased in many organs, (2) the abundance of phospholipids containing MUFA decreased, (3) the abundance of TG and phospholipids containing PUFA increased, and (4) the most prominent change in the lipidome was found in the kidney with aging. Although similar results of PUFA/MUFA ratio have been reported in plasma and serum lipidomics studies, our results indicate that the tendency of PUFA and MUFA metabolism is a common phenomenon of aging in organs examined in this study. The unique enrichment of BMP-containing PUFAs is worth noting because only few reports have investigated the age dependency of BMP. BMP lipid is enriched in late endosomes and lysosomes, and it promotes the enzymatic activity of acidic sphingomyelinase (ASM) by direct binding[63]. Cellular senescence is associated with lysosomal homeostasis. Cytosolic pH change is associated with cellular senescence induced by lysosomal membrane damage[64], and ASM activity is elevated with aging[65]. Therefore, the age-dependent increase in BMP may be related to lysosomal membrane homeostasis and subsequent cellular senescence in tissues.

We identified many unique changes in the lipidome during aging in a sex- or microbiome-dependent manner. Microbiota-dependent lipid changes were observed in the feces, small intestine, and large intestine. Interestingly, microbiome-dependent changes in BA and SL were observed in remote organs, except for the bone marrow. It is well known that cleavage of conjugated moieties in bile acids is usually performed by the gut microbiota. Thus, the difference in the SPF/GF ratio between conjugated and unconjugated bile acids is likely to reflect the effect of the enzyme activities of the microbiome. The mechanism of the unique translocation of SL into various tissues is unclear when considering the fact that most of the other microbiota-derived lipids such as *N*-acyl amides, PI ceramides, and PE ceramides were not detected in remote organs. The genera *Alistipes* and *Odoribacter* produce SLs, whose molecules have bioactivities, such as antagonistic action on von Willebrand factor receptors, cytotoxicity in cancer cells, inhibitory functions of DNA polymerase, and anti-inflammatory effect[38]. *Alistipes* is relevant to dysbiosis and disease, and contrasting evidence of its pathogenicity has been reported; it has protective effects against liver fibrosis, colitis, and cardiovascular disease and is associated with colorectal cancer and mental signs of depression[66]. To investigate the mechanism in detail, the development of databases organizing the pair of commensal lipids and their producers is indispensable, along with metagenome sequences for multiple organs. Moreover, MS-imaging should provide new insights into the local distribution and biological importance of SL for the understanding of host and microbiome relationships.

Integrated analysis of the kidney transcriptome and lipidome revealed the relevance between gene expression and lipidome from the viewpoint of SPF/GF and male/female differences. Age-dependent decreases in ether-linked glycerolipids, including ether PC, ether PI, ether PS, ether DG, and ether MGDG, were clearly observed in male kidneys, and their profiles correlated with the expression levels of AGPS and FAR1. Based on the profile of PE species in which the alkyl and alkenyl types can be distinguished by the ESI(+)-MS/MS spectrum, the ether link often consists of an alkenyl (plasmalogen) type whose vinyl ether moiety has antioxidant activity[67]. The decrease of these metabolites in aging is considered the functional attenuation of cellular organelle peroxisomes as enriched in the GO analysis of male-specific transcriptome data. In addition, our results indicate that galactosyl lipid metabolism in the kidney is highly correlated with the expression level of UGT8a. Although the machinery responsible for MGDG and DGDG biosynthesis in mammalian cells is not fully understood, recombinant expression of UGT8a in CHO cells tends to enrich the MGDG lipid[55,56], indicating that both galactosyl ceramides and galactosyl glycerides can be synthesized via UGT8a enzymatic activity. While *Ugt8a* knock-out mice exhibit pronounced tremor and progressive ataxia, no major morphological or functional defects are reported in the kidney[68,69]. The biological importance of MGDG in the kidney should be investigated in the future.

Furthermore, gene expression is regulated in the kidney by TFs including AR and STAT3 and active histone marks (H3K9ac, H3K27ac, and H3K4me3) according to the proposal of ChIP-Atlas. Of these, STAT3 was identified as the most significantly enriched TF in the ChIP-Atlas program, and human FAR1 and UGT8 are predicted to be target genes of STAT3[60]. However, the UGT8 gene is not predicted to be the target of other STAT family members. We further ascertained the consistency of the sequences recognized by STAT3 in humans and mice, whose matrix IDs of JASPAR are MA0144.2 and MA0144.1, respectively[70]. Based on the sequence information of the promoter regions of human UGT8 and mouse UGT8a, a high-scoring STAT3-binding sequence was detected using the JASPAR program. These results indicate that the substantial changes in glycolipids between male and female mice may be explained by the age- and sex-dependent AR-STAT3 TF activity that regulates the expression profile of UGT8a in the kidney. Moreover, age-dependent increases in Gal2Cer and Hex3Cer were observed. As observed in Fabry disease, which is caused by deficiency or decreased activity of α-galactosidase A (GLA), an intracellular lysosomal enzyme, the abnormal accumulation of Hex3Cer causes severe renal damage[71]. Given that the gene expression level of GLA did not change between males and females and between aged and young mice, the accumulation of these glycolipids may be due to activity increase of the biosynthetic enzymes, dysfunction of intracellular organelles such as lysosomes, or other mechanisms that maintain metabolic homeostasis. While a few changes in gene expression between SPF and GF were observed in the kidney, we identified several correlations between microbiota-derived lipids and the host transcriptome, the causality of which will be investigated in the future.

This study provides new insights into the potential link between lipid metabolism and aging. While the biological importance of lipid metabolites described in this study will be further investigated, other layers of omics data, such as proteomics and metagenomics, will be required to examine the harmonized

mechanism of host and bacterial lipid metabolism. In particular, it is important to perform integrated analysis also in the liver and intestinal tract, since the functions of these organs are considered to be substantially influenced by aging and intestinal microbiota[72]. It is also important to translate the results of mice to human to consider the extensibility of our findings. Moreover, annotation of unknown spectra is needed because more than 200 unique and highly abundant peaks remain unknown in the present study. The open sharing of MS raw data will facilitate further annotation with the updates of computational mass, which is an active research field in metabolomics and lipidomics[73,74]. Further data accumulation, biochemical validation, and informatics research will lead to a better understanding of the molecular mechanisms underlying cellular senescence and age-related chronic diseases, and will contribute to build a foundation for establishing a healthy and long-living society.

Declarations

Acknowledgements

This work was supported by the JSPS Grant-in-Aid for Scientific Research on Innovative Areas “Biology of LipoQuality” (15H05897 and 15H05898 to M.A.), JSPS KAKENHI (21K18216 to Hiroshi T., 20H00495 to M.A.), the National Cancer Center Research and Development Fund (2020-A-9, H.T.), AMED Japan Program for Infectious Diseases Research and Infrastructure (21wm0325036h0001, H.T. and M.A.), JST National Bioscience Database Center (NBDC, H.T.), JST ERATO “Arita Lipidome Atlas Project” (JPMJER2101 to H.T. and M.A.), and RIKEN Aging Project Program (M.A. and A.M.).

Author contributions

H.T., T.I. A.M. and M.A. designed the study. H.T. and M.T. developed MS-DIAL annotation system. T.I. prepared the biological samples and T.I. and H.A. performed LC-MS experiments. K.O. and S.I. performed the transcriptome analysis of kidney. Y.Y. developed RIKEN lipidomics database. H.T. and M.A. wrote the manuscript. All authors have thoroughly discussed this project and helped improve the manuscript.

Data availability

All raw MS data are freely available on the RIKEN DROP Met website (http://prime.psc.riken.jp/menta.cgi/prime/drop_index), under index number DM0044. The lipidomic results are recorded in **Supplementary Data 1**, and they can be browsed in our RIKEN lipidomics database (http://prime.psc.riken.jp/menta.cgi/lipidomics/index). The RNA-seq raw data is available on the DDBJ webpage, under the identifier of PRJDB14285. The transcriptome result is recorded in **Supplementary Data 2**. The source data for Figures is also recorded as **Source Data**.

References

1. Harayama, T. & Riezman, H. Understanding the diversity of membrane lipid composition. *Nat Rev Mol Cell Biol* **19**, 281-296 (2018).

2. Soehnlein, O. & Libby, P. Targeting inflammation in atherosclerosis - from experimental insights to the clinic. *Nat Rev Drug Discov* **20**, 589-610 (2021).

3. Snaebjornsson, M.T., Janaki-Raman, S. & Schulze, A. Greasing the Wheels of the Cancer Machine: The Role of Lipid Metabolism in Cancer. *Cell Metab* **31**, 62-76 (2020).

4. Huby, T. & Gautier, E.L. Immune cell-mediated features of non-alcoholic steatohepatitis. *Nat Rev Immunol* **22**, 429-443 (2022).

5. Baek, J., He, C.C., Afshinnia, F., Michailidis, G. & Pennathur, S. Lipidomic approaches to dissect dysregulated lipid metabolism in kidney disease. *Nat Rev Nephrol* **18**, 38-55 (2022).

6. Johnson, A.A. & Stolzing, A. The role of lipid metabolism in aging, lifespan regulation, and age-related disease. *Aging Cell* **18**, e13048 (2019).

7. Khosla, S., Farr, J.N., Tchkonia, T. & Kirkland, J.L. The role of cellular senescence in ageing and endocrine disease. *Nat Rev Endocrinol* **16**, 263-275 (2020).

8. Ferrucci, L. & Fabbri, E. Inflammageing: chronic inflammation in ageing, cardiovascular disease, and frailty. *Nat Rev Cardiol* **15**, 505-522 (2018).

9. Mutlu, A.S., Duffy, J. & Wang, M.C. Lipid metabolism and lipid signals in aging and longevity. *Dev Cell* **56**, 1394-1407 (2021).

10. Sacket, S.J., Chung, H.Y., Okajima, F. & Im, D.S. Increase in sphingolipid catabolic enzyme activity during aging. *Acta Pharmacol Sin* **30**, 1454-1461 (2009).

11. Mielke, M.M.*, et al.* Serum ceramides increase the risk of Alzheimer disease The Women's Health and Aging Study II. *Neurology* **79**, 633-641 (2012).

12. Streeper, R.S.*, et al.* Deficiency of the lipid synthesis enzyme, DGAT1, extends longevity in mice. *Aging (Albany NY)* **4**, 13-27 (2012).

13. Su, L.J.*, et al.* Reactive Oxygen Species-Induced Lipid Peroxidation in Apoptosis, Autophagy, and Ferroptosis. *Oxid Med Cell Longev* **2019**, 5080843 (2019).

14. Ponnappan, U., Holley, D.H. & Lipschitz, D.A. Effect of age on the fatty acid composition of phospholipids in human lymphocytes. *Exp Gerontol* **31**, 125-133 (1996).

15. Rabini, R.A., *et al.* Reduced susceptibility to peroxidation of erythrocyte plasma membranes from centenarians. *Exp Gerontol* **37**, 657-663 (2002).

16. Mitchell, T.W., Buffenstein, R. & Hulbert, A.J. Membrane phospholipid composition may contribute to exceptional longevity of the naked mole-rat (Heterocephalus glaber): A comparative study using shotgun lipidomics. *Exp Gerontol* **42**, 1053-1062 (2007).

17. Nagpal, R., *et al.* Gut microbiome and aging: Physiological and mechanistic insights. *Nutr Healthy Aging* **4**, 267-285 (2018).

18. Albouery, M., *et al.* Age-Related Changes in the Gut Microbiota Modify Brain Lipid Composition. *Front Cell Infect Mi* **9**(2020).

19. Naoe, S., Tsugawa, H., Takahashi, M., Ikeda, K. & Arita, M. Characterization of Lipid Profiles after Dietary Intake of Polyunsaturated Fatty Acids Using Integrated Untargeted and Targeted Lipidomics. *Metabolites* **9**(2019).

20. Weger, B.D., *et al.* The Mouse Microbiome Is Required for Sex-Specific Diurnal Rhythms of Gene Expression and Metabolism. *Cell Metab* **29**, 362-+ (2019).

21. Yasuda, S., *et al.* Elucidation of Gut Microbiota-Associated Lipids Using LC-MS/MS and 16S rRNA Sequence Analyses. *Iscience* **23**(2020).

22. Ghorasaini, M., *et al.* Cross-Laboratory Standardization of Preclinical Lipidomics Using Differential Mobility Spectrometry and Multiple Reaction Monitoring. *Anal Chem* **93**, 16369-16378 (2021).

23. Tsugawa, H., *et al.* A lipidome atlas in MS-DIAL 4. *Nat Biotechnol* **38**, 1159-+ (2020).

24. Gonzalez-Covarrubias, V. Lipidomics in longevity and healthy aging. *Biogerontology* **14**, 663-672 (2013).

25. Slade, E., *et al.* Age and sex are associated with the plasma lipidome: findings from the GOLDN study. *Lipids Health Dis* **20**(2021).

26. Beyene, H.B., *et al.* High-coverage plasma lipidomics reveals novel sex-specific lipidomic fingerprints of age and BMI: Evidence from two large population cohort studies (vol 18, e3000870, 2020). *Plos Biol* **18**(2020).

27. Eum, J.Y., *et al.* Aging-related lipidomic changes in mouse serum, kidney, and heart by nanoflow ultrahigh-performance liquid chromatography-tandem mass spectrometry. *J Chromatogr A* **1618**(2020).

28. Papsdorf, K. & Brunet, A. Linking Lipid Metabolism to Chromatin Regulation in Aging. *Trends Cell Biol* **29**, 97-116 (2019).

29. Pollard, A.K., Ortori, C.A., Stoger, R., Barrett, D.A. & Chakrabarti, L. Mouse mitochondrial lipid composition is defined by age in brain and muscle. *Aging-Us* **9**, 986-998 (2017).

30. Ding, J.*, et al.* A metabolome atlas of the aging mouse brain. *Nat Commun* **12**(2021).

31. Okahashi, N., Ueda, M., Yasuda, S., Tsugawa, H. & Arita, M. Global profiling of gut microbiota-associated lipid metabolites in antibiotic-treated mice by LC-MS/MS-based analyses. *STAR Protoc* **2**, 100492 (2021).

32. Velagapudi, V.R.*, et al.* The gut microbiota modulates host energy and lipid metabolism in mice. *J Lipid Res* **51**, 1101-1112 (2010).

33. Grabner, G.F.*, et al.* Metabolic regulation of the lysosomal cofactor bis(monoacylglycero)phosphate in mice. *Journal of Lipid Research* **61**, 995-1003 (2020).

34. Showalter, M.R.*, et al.* The Emerging and Diverse Roles of Bis(monoacylglycero) Phosphate Lipids in Cellular Physiology and Disease. *Int J Mol Sci* **21**(2020).

35. Jojima, K., Edagawa, M., Sawai, M., Ohno, Y. & Kihara, A. Biosynthesis of the anti-lipid-microdomain sphingoid base 4,14-sphingadiene by the ceramide desaturase FADS3. *Faseb J* **34**, 3318-3335 (2020).

36. Pergande, M.R.*, et al.* Lipidomic analysis identifies age-disease-related changes and potential new biomarkers in brain-derived extracellular vesicles from metachromatic leukodystrophy mice. *Lipids Health Dis* **21**(2022).

37. Slomiany, B.L., Murty, V.L.N., Liau, Y.H. & Slomiany, A. Animal Glycoglycerolipids. *Prog Lipid Res* **26**, 29-51 (1987).

38. Walker, A.*, et al.* Sulfonolipids as novel metabolite markers of Alistipes and Odoribacter affected by high-fat diets. *Sci Rep-Uk* **7**(2017).

39. Wang, Y.*, et al.* Sex differences in transcriptomic profiles in aged kidney cells of renin lineage. *Aging (Albany NY)* **10**, 606-621 (2018).

40. Sembach, F.E.*, et al.* Impact of sex on diabetic nephropathy and the renal transcriptome in UNx db/db C57BLKS mice. *Physiol Rep* **7**, e14333 (2019).

41. Braun, F.*, et al.* Altered lipid metabolism in the aging kidney identified by three layered omic analysis. *Aging (Albany NY)* **8**, 441-457 (2016).

42. Reimand, J.*, et al.* Pathway enrichment analysis and visualization of omics data using g:Profiler, GSEA, Cytoscape and EnrichmentMap. *Nat Protoc* **14**, 482-517 (2019).

43. Carrero, J.J., Hecking, M., Chesnaye, N.C. & Jager, K.J. Sex and gender disparities in the epidemiology and outcomes of chronic kidney disease. *Nat Rev Nephrol* **14**, 151-164 (2018).

44. Zou, Z.N., Ohta, T., Miura, F. & Oki, S. ChIP-Atlas 2021 update: a data-mining suite for exploring epigenomic landscapes by fully integrating ChIP-seq, ATAC-seq and Bisulfite-seq data. *Nucleic Acids Res* **50**, W175-W182 (2022).

45. Martovetsky, G., Tee, J.B. & Nigam, S.K. Hepatocyte nuclear factors 4alpha and 1alpha regulate kidney developmental expression of drug-metabolizing enzymes and drug transporters. *Mol Pharmacol* **84**, 808-823 (2013).

46. Chamouton, J. & Latruffe, N. PPARalpha/HNF4alpha interplay on diversified responsive elements. Relevance in the regulation of liver peroxisomal fatty acid catabolism. *Curr Drug Metab* **13**, 1436-1453 (2012).

47. Harris, A.N., Castro, R.A., Lee, H.W., Verlander, J.W. & Weiner, I.D. Role of the renal androgen receptor in sex differences in ammonia metabolism. *Am J Physiol-Renal* **321**, F629-F644 (2021).

48. O'Brown, Z.K., Van Nostrand, E.L., Higgins, J.P. & Kim, S.K. The Inflammatory Transcription Factors NFkappaB, STAT1 and STAT3 Drive Age-Associated Transcriptional Changes in the Human Kidney. *PLoS Genet* **11**, e1005734 (2015).

49. Liu, M.*, et al.* Androgen-STAT3 activation may contribute to gender disparity in human simply renal cysts. *Int J Clin Exp Patho* **6**, 686-694 (2013).

50. Iida, K.*, et al.* A Possible Role of Vitamin-D Receptors in Regulating Vitamin-D Activation in the Kidney. *P Natl Acad Sci USA* **92**, 6112-6116 (1995).

51. Cozzolino, M. & Malindretos, P. The role of vitamin D receptor activation in chronic kidney disease. *Hippokratia* **14**, 7-9 (2010).

52. Langfelder, P. & Horvath, S. WGCNA: an R package for weighted correlation network analysis. *Bmc Bioinformatics* **9**(2008).

53. Molenaar, M.R.*, et al.* LION/web: a web-based ontology enrichment tool for lipidomic data analysis. *Gigascience* **8**(2019).

54. Muralidharan, S.*, et al.* A reference map of sphingolipids in murine tissues. *Cell Rep* **35**(2021).

55. van der Bijl, P., Strous, G.J., LopesCardozo, M., ThomasOates, J. & van Meer, G. Synthesis of non-hydroxy-galactosylceramides and galactosyldiglycerides by hydroxy-ceramide galactosyltransferase. *Biochem J* **317**, 589-597 (1996).

56. Hayashi, T., Hayashi, E., Fujimoto, M., Sprong, H. & Su, T.P. The Lifetime of UDP-galactose: Ceramide Galactosyltransferase Is Controlled by a Distinct Endoplasmic Reticulum-associated Degradation (ERAD) Regulated by Sigma-1 Receptor Chaperones. *J Biol Chem* **287**, 43156-43169 (2012).

57. Lu, C.L.*, et al.* Indoxyl-Sulfate-Induced Redox Imbalance in Chronic Kidney Disease. *Antioxidants (Basel)* **10**(2021).

58. Strott, C.A. & Higashi, Y. Cholesterol sulfate in human physiology: what's it all about? *J Lipid Res* **44**, 1268-1278 (2003).

59. Stofan, M. & Guo, G.L. Bile Acids and FXR: Novel Targets for Liver Diseases. *Front Med-Lausanne* **7**(2020).

60. Rouillard, A.D.*, et al.* The harmonizome: a collection of processed datasets gathered to serve and mine knowledge about genes and proteins. *Database-Oxford* (2016).

61. Dayama, G., Priya, S., Niccum, D.E., Khoruts, A. & Blekhman, R. Interactions between the gut microbiome and host gene regulation in cystic fibrosis. *Genome Med* **12**(2020).

62. Ohsaka, F.*, et al.* Gut commensals suppress interleukin-2 production through microRNA-200/BCL11B and microRNA-200/ETS-1 axes in lamina propria leukocytes of murine large intestine. *Biochem Biophys Res Commun* **534**, 808-814 (2021).

63. Kolter, T. & Sandhoff, K. Lysosomal degradation of membrane lipids. *Febs Lett* **584**, 1700-1712 (2010).

64. Johmura, Y.*, et al.* Senolysis by glutaminolysis inhibition ameliorates various age-associated disorders. *Science* **371**, 265-+ (2021).

65. Babenko, N.A., Garkavenko, V.V., Storozhenko, G.V. & Timofiychuk, O.A. Role of acid sphingomyelinase in the age-dependent dysregulation of sphingolipids turnover in the tissues of rats. *Gen Physiol Biophys* **35**, 195-205 (2016).

66. Parker, B.J., Wearsch, P.A., Veloo, A.C.M. & Rodriguez-Palacios, A. The Genus Alistipes: Gut Bacteria With Emerging Implications to Inflammation, Cancer, and Mental Health. *Front Immunol* **11**, 906 (2020).

67. Almsherqi, Z.A. Potential Role of Plasmalogens in the Modulation of Biomembrane Morphology. *Front Cell Dev Biol* **9**(2021).

68. Tadano-Aritomi, K.*, et al.* Kidney lipids in galactosylceramide synthase-deficient mice: absence of galactosylsulfatide and compensatory increase in more polar sulfoglycolipids. *Journal of Lipid Research* **41**, 1237-1243 (2000).

69. Honke, K., *et al.* Paranodal junction formation and spermatogenesis require sulfoglycolipids. *P Natl Acad Sci USA* **99**, 4227-4232 (2002).

70. Stormo, G.D. Modeling the specificity of protein-DNA interactions. *Quant Biol* **1**, 115-130 (2013).

71. Thelen, A.M. & Zoncu, R. Emerging Roles for the Lysosome in Lipid Metabolism. *Trends Cell Biol* **27**, 833-850 (2017).

72. Fan, Y. & Pedersen, O. Gut microbiota in human metabolic health and disease. *Nat Rev Microbiol* **19**, 55-71 (2021).

73. Tsugawa, H., Rai, A., Saito, K. & Nakabayashi, R. Metabolomics and complementary techniques to investigate the plant phytochemical cosmos. *Nat Prod Rep* **38**, 1729-1759 (2021).

74. McDonald, J.G., *et al.* Introducing the Lipidomics Minimal Reporting Checklist. *Nat Metab* (2022).

Figures

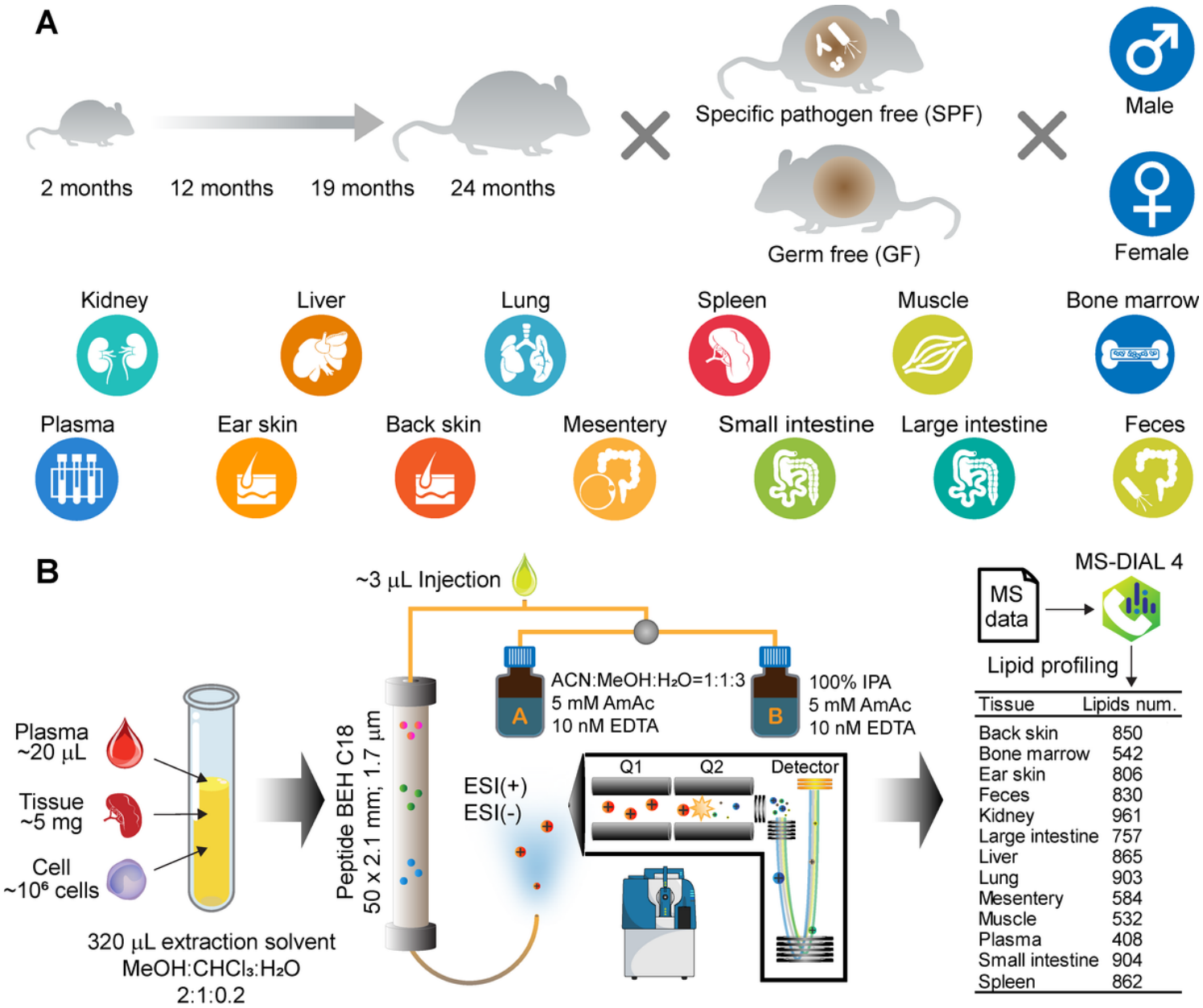

Figure 1

Summary of experimental design and lipid profiling in this study. (a) Four types of mice were prepared: male and SPF (specific pathogen-free), male and GF (germ free), female and SPF, and female and GF. Total 13 biospecimens were harvested at 2 months, 12 months (1 year), 19 months, and 24 months (2 years). (b) The lipid extraction was performed for the optimal volume of biological samples. The untargeted lipidomics data was obtained by our experimental condition. The mass spectrometry data was analyzed by the MS-DIAL 4.20 algorithm with the updated lipid libraries.

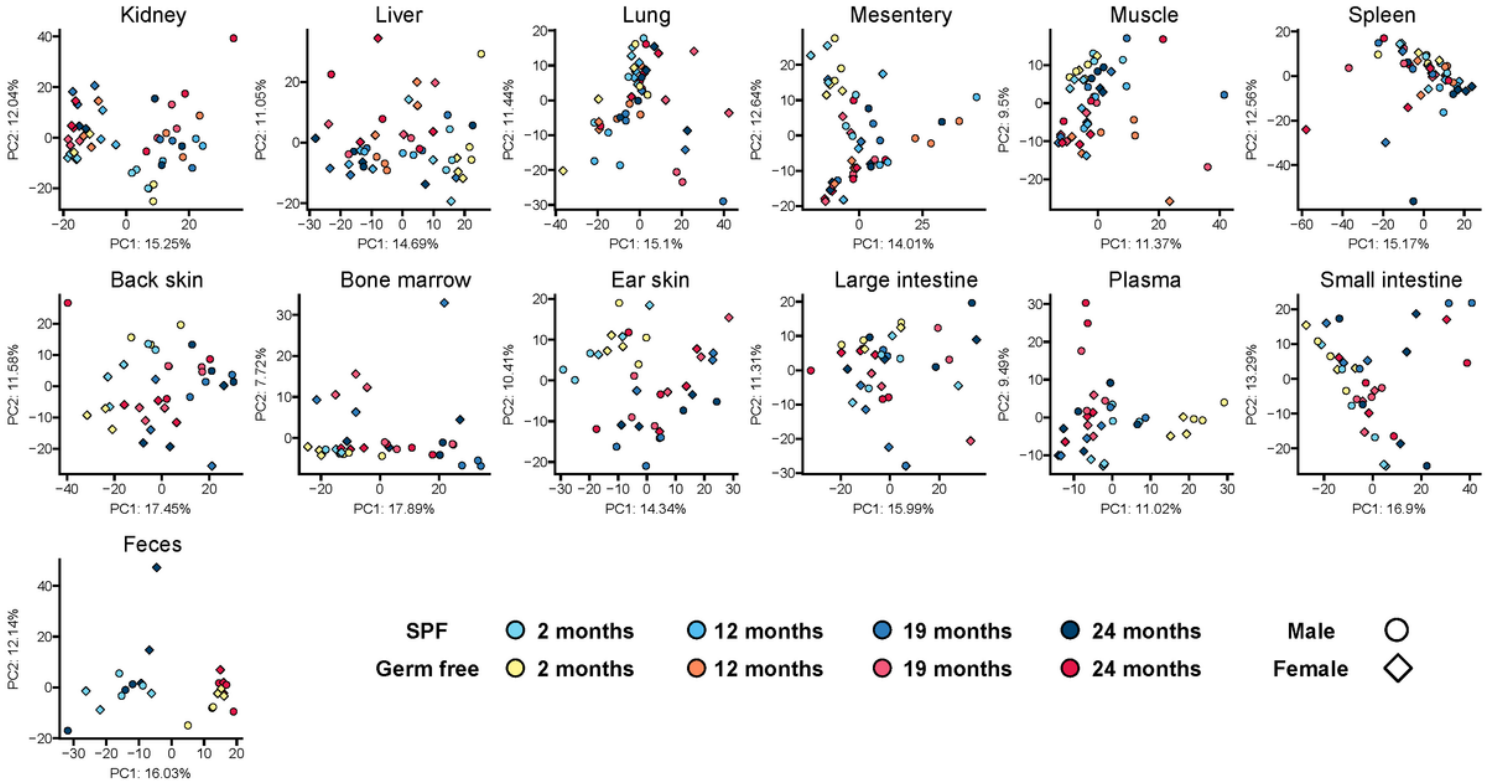

Figure 2

Results of principal component analysis for 13 biological samples. The auto-scaling was performed prior to the calculation of the PCA score and loading values. The X and Y axes describe the first and second PCs with the contributed ratios. The blue and red color gradients indicate SPF and germ-free mice (with aging), respectively. The circle and diamond symbols indicate male and female, respectively.

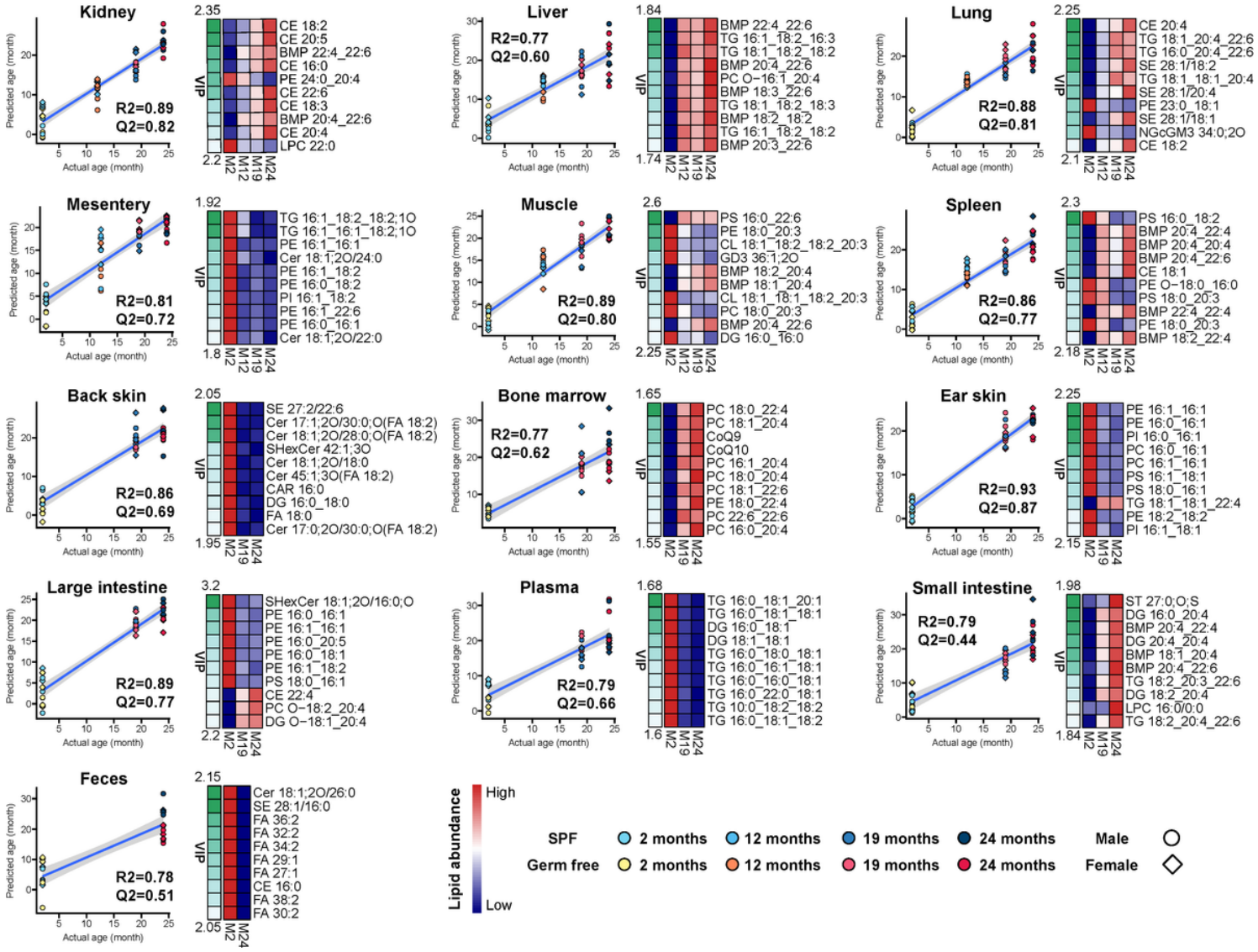

Figure 3

Investigation of age-related lipid changes using orthogonal partial least square regression (OPLS-R). The auto-scaled lipidome data was subjected to the OPLS-R model construction. The model was evaluated by the R-square (R^2) and Q-square (Q^2) values. The top 10 variable importance for prediction (VIP) values of metabolites whose chromatographic peak shape retained singlet and better symmetry were described. The same symbol and color gradients as those of PCA were used.

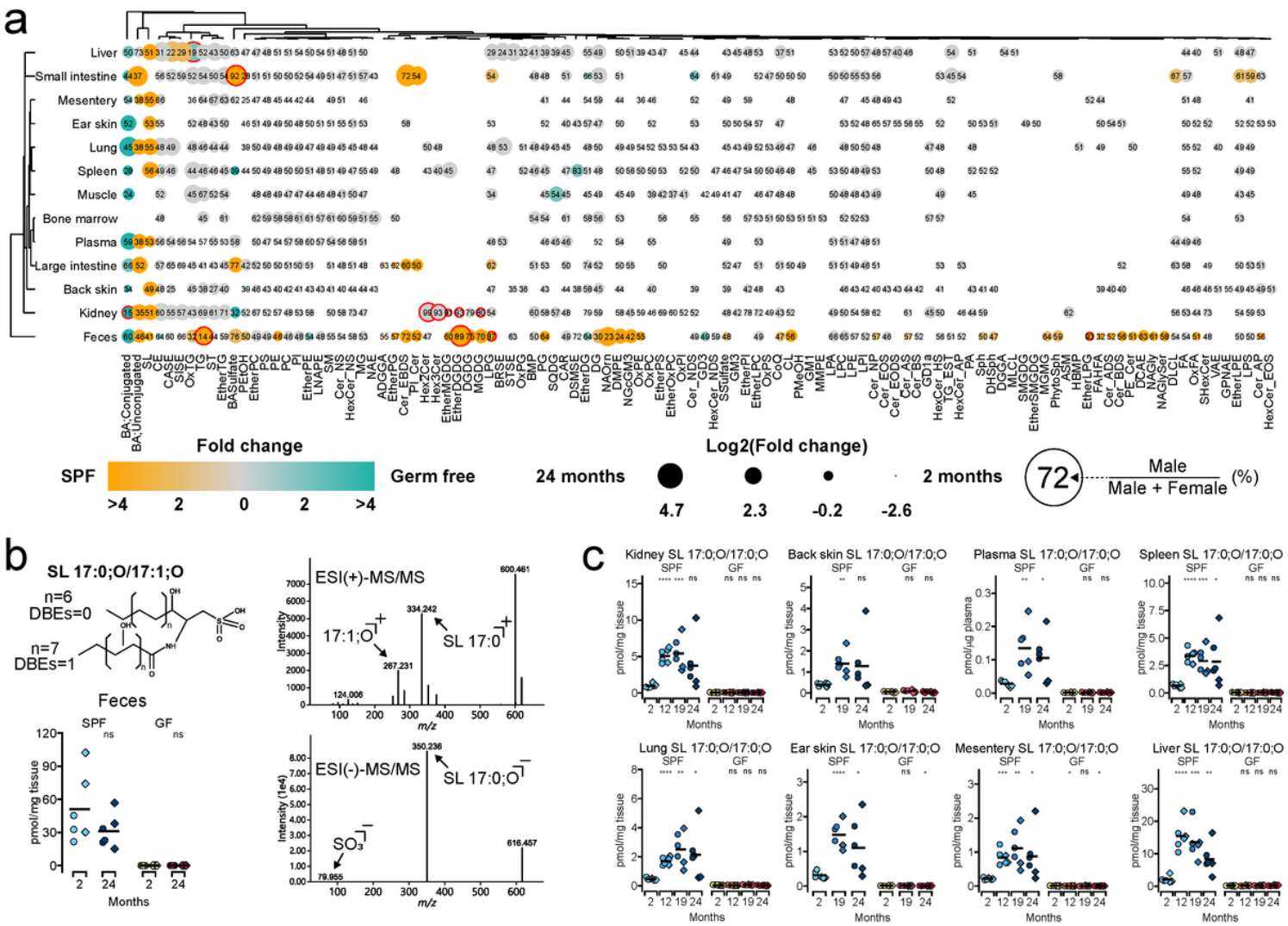

Figure 4

The overview of lipidomes. (a) X-axis and y-axis show lipid subclass and sample name, respectively. The circle size reflects the fold changes of 24 months over 2 months. The gradient color from green to orange represents the ratio of SPF and GF. The number in each circle shows the ratio of male/(male + female), and the red outline indicates the ratio of >80% or <20%. The values were calculated by the semi-quantitative values of lipids. (b) The profile and MS/MS spectra of sulfonolipid (SL) containing sphingobase 17:0;O and *N*-acyl chain 17:1;O in fecal sample were described. (c) The lipid profiles of SL 17:0;O/17:0;O, which is the most abundant molecule in all tissues, were described. The *p*-value was calculated by Dunnett's test. $^{*}P < 0.05$, $^{**}P < 0.01$, and $^{***}P < 0.001$ against 2 months.

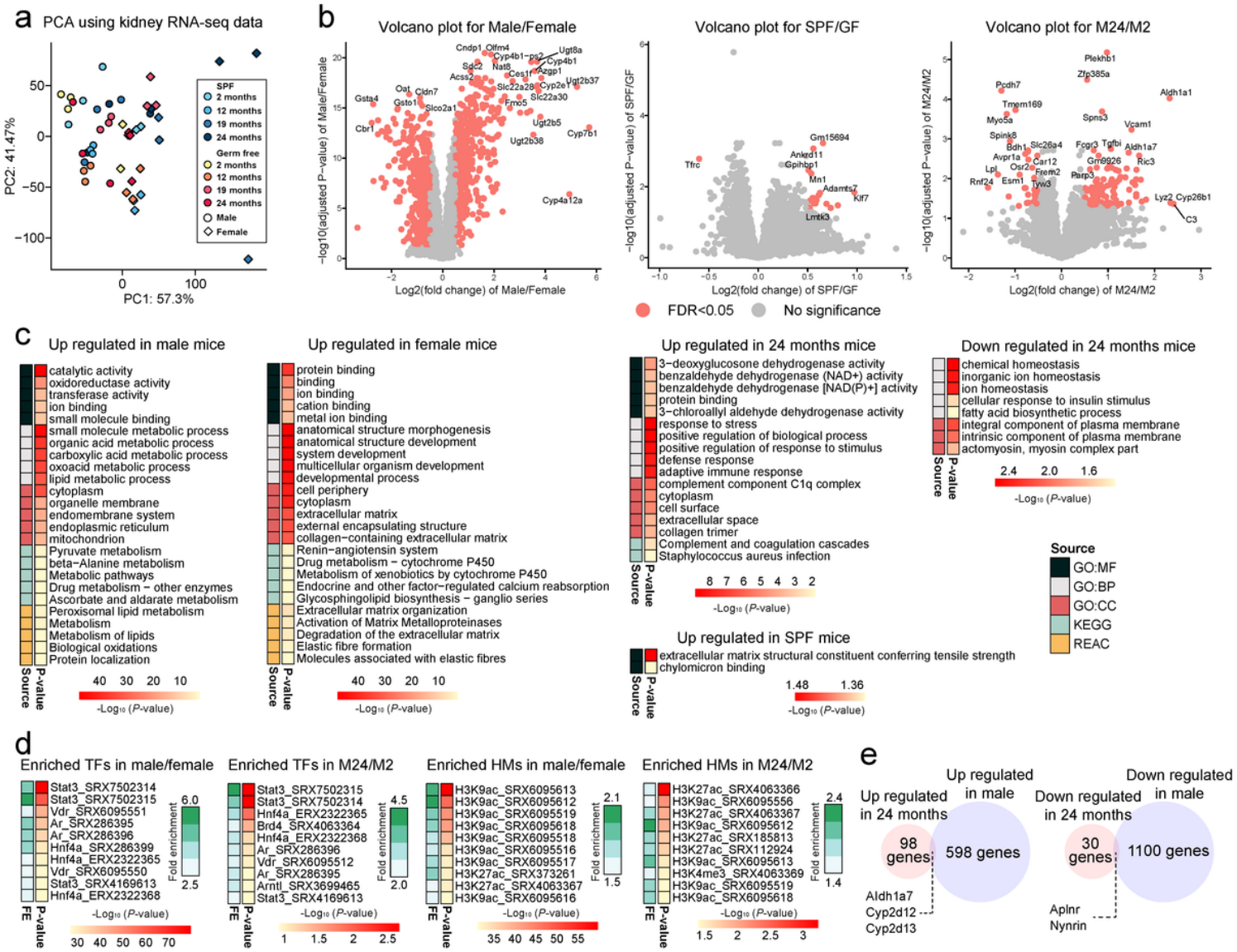

Figure 5

Data interpretation of kidney transcriptome. (a) The score plot of PCA using the kidney transcriptome data. The data normalization was performed by the DEseq2 package, and the auto-scaling was used for the data transformation. X and Y axes show the first and second principal components. (b) The volcano plots show male versus female, SPF versus GF, and aged (24 months; M24) versus young (two months; M2) mice. The X and Y axes show the log2 transformed fold change and minus log10 transformed *p*-value, respectively. The upregulated genes in male, SPF, and M24 represent the positive value on the X-axis. Red circle indicates significance that is defined at the condition of >0.5 of log2 fold change and <0.05 adjusted *p*-value. The *p*-value was adjusted by Benjamini-Hochberg method. (c) The result of gene ontology (GO) analysis.The significant genes in the volcano plots (Fig. 5c) were applied to the g:Profiler program. The gene ontology source of molecular function, biological process, and cellular component, in addition to the pathway ontology source of KEGG and Reactome databases, were shown. The top five significantly enriched ontology teams in each GO source were described with the *p*-value. (d) The investigation of transcription factors (TFs) and histone modifications that regulate the significant

genes.The enrichment analysis of ChiP-Atlas was used at *Mus musculus* (mm 10) and the cell type of kidney with the default parameter setting, and the top 10 enriched terms were described. The TF name and the data source index were described. (e) The investigation of commonly up or downregulated genes in male and aged mice. The result was described as the Venn diagram.

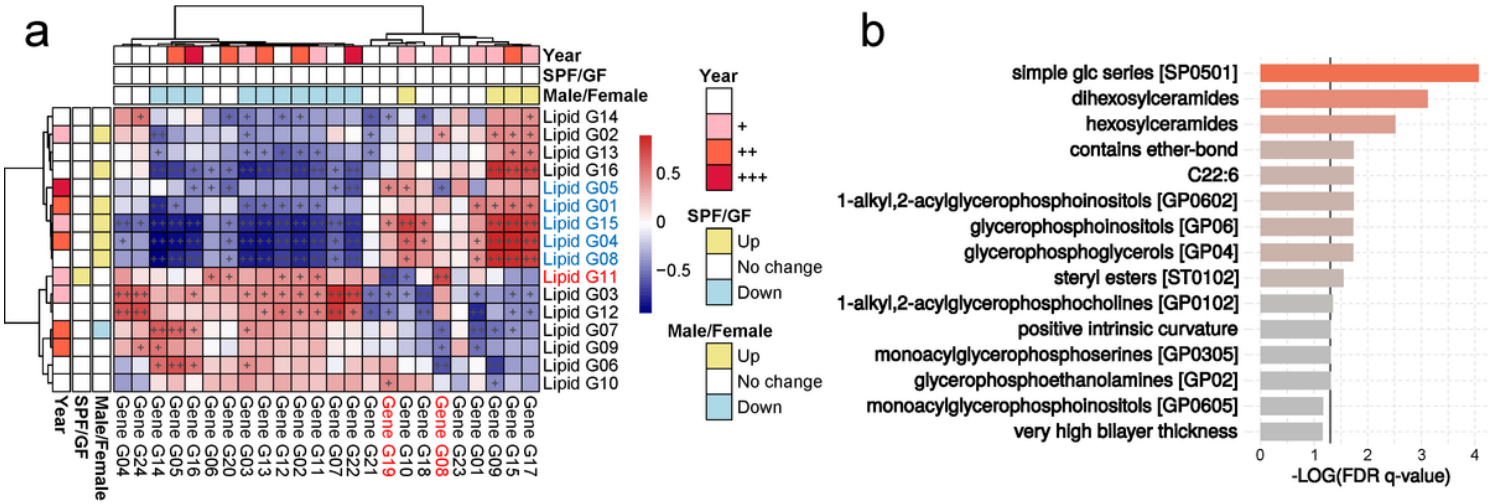

Figure 6

The integrated analysis of transcriptome and lipidome data. (a) The weighted correlation network analysis was used to integrate the lipidome and transcriptome data. The statistical significance for the parameters of aging, SPF/GF, and male/female was evaluated by the median profile of molecules contained in the same cluster. The *p*-value was adjusted by the false discovery rate method. The results of the *p*-values for the difference between the sexes and the presence or absence of intestinal bacteria were considered significant if the value was less than 0.05. Yellow color indicates elevation in SPF or male mice, and blue color indicates elevation in GF or female mice. The clusters highlighted by blue color were applied to the ontology analysis, and the clusters highlighted by red color were used in the correlation analysis of microbiota related genes and lipids (Fig. 8). The significance of gene and lipid correlations was evaluated by $+R^2 > 0.4$ and $++R^2 > 0.6$. For year (aging) property, the *p*-value was calculated by the partial correlation analysis adjusted by sex and microbiome properties. $+P < 0.05$, $++P < 0.01$, and $+++P < 0.001$. (b) The result of lipid ontology enrichment analysis. The data matrix consisting of lipid metabolites represented by blue clusters in Figure 6a was applied to the LION/web. The enrichment terms were evaluated by the analysis of variance values from four groups M24/male, M24/female, M2/male, and M2/female.

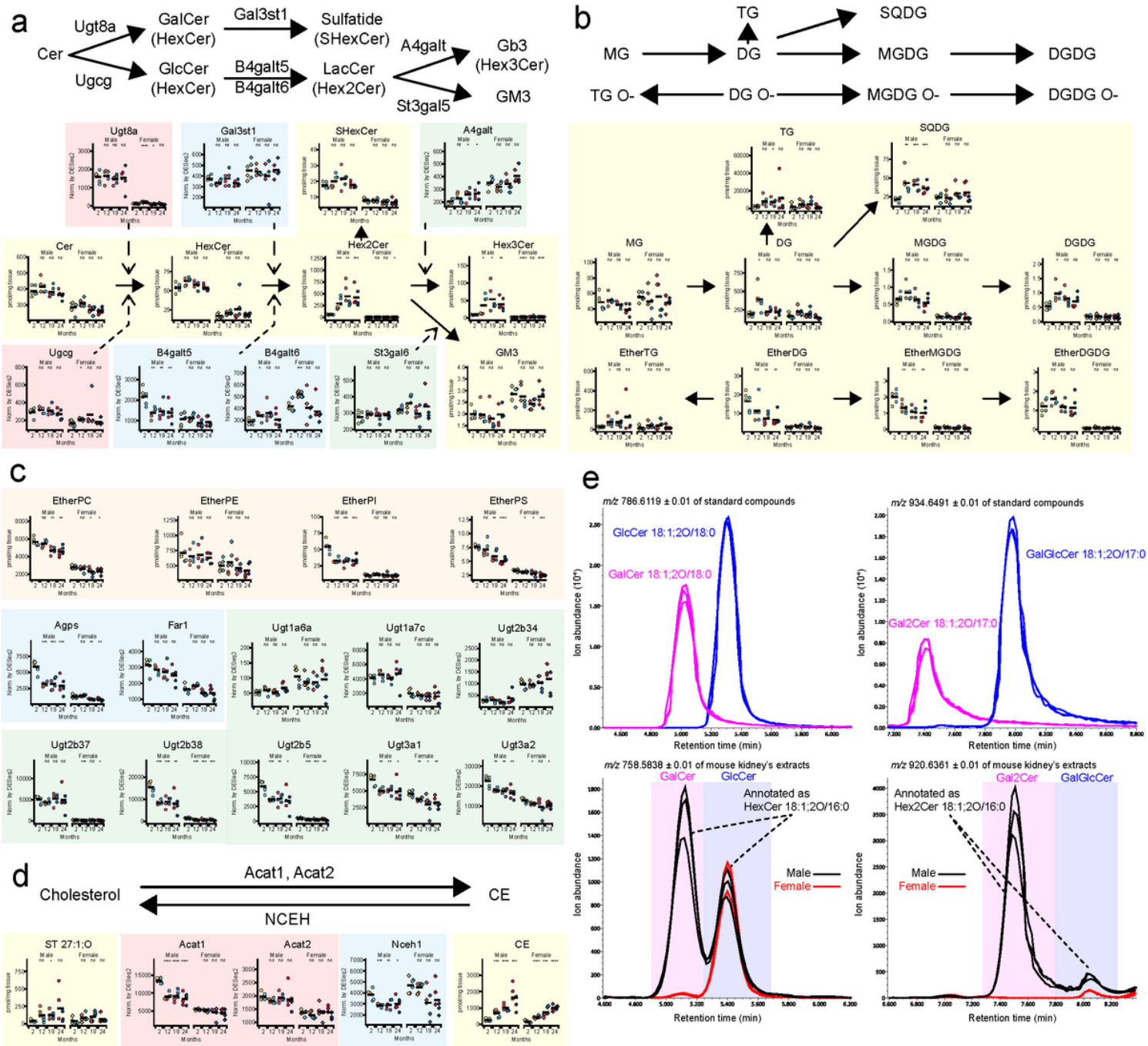

Figure 7

The lipid metabolic pathways of glycolipids and sterol esters. (a) The metabolic pathway of glycosyl ceramides. The quantification of each lipid subclass was performed by summing the quantitative values of lipid molecules classified to the lipid subclasses. Both the lipid- and gene profiles with the metabolic pathways were mapped as dot plots. (b) The metabolic pathway of glycosyl glycerolipids. (c) The metabolic pathway of ether-linked (alkylacyl) glycerophospholipids, the significant genes related to the alkylacyl phospholipids, and the other UGT genes, which were expected to be related to glycosyl lipid metabolism. (d) The pathway of sterol and steryl ester metabolism. The definition of symbol and color in the dot plot is the same as Figure 1. The *p*-value was calculated by Dunnett's test. **P*< 0.05, ***P*< 0.01, and ****P*< 0.001 against 2 months. (e) Blue and pink colors represent the extracted ion chromatograms

(EICs) of authentic standards β-glucosyl ceramide 18:1(4E)(1OH,3OH)/18:0 and β-galactosyl ceramide 18:1(4E)(1OH,3OH)/18:0 at the top-left panel, respectively. Same colors represent the EICs of β-lactosyl ceramide 18:1(4E)(1OH,3OH)/17:0 and β-galabiosyl ceramide 18:1(4E)(1OH,3OH)/17:0 at the top-right panel, respectively. Black and red colors indicate the EICs of ammonium adduct form of HexCer 18:1;2O/16:0 for male and female mice at the bottom-left panel, respectively. Same colors indicate the EICs of ammonium adduct form of Hex2Cer 18:1;2O/16:0 for male and female mice at the bottom-right panel, respectively. Three technical and biological replicates were prepared for authentic standards and kidney tissue extracts, respectively.

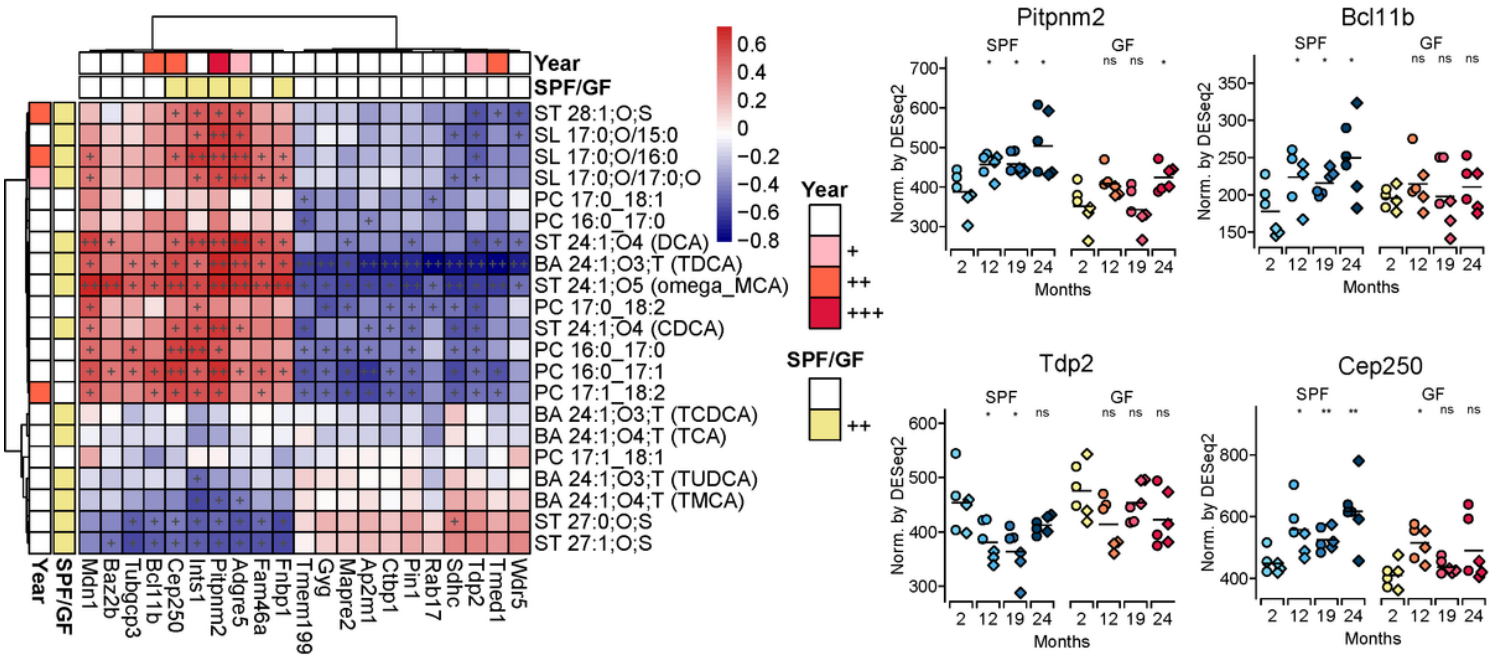

Figure 8

The correlation of genes with the lipid metabolites associated to gut microbiota. The definitions of statistical significances with year (aging), SPF/GF, and gene-lipid correlation are the same as those of Figure 6. Several bile acids were identified by the authentic standards. Dot plots indicate the significantly changed genes only in SPF mice with aging. . The *p*-value was calculated by Dunnett's test. *$P < 0.05$, **$P < 0.01$ against 2 months.

Supplementary Files

This is a list of supplementary files associated with this preprint. Click to download.

- Tsugawaetalaginglipidomicssupplementaryinformation.docx
- SupplementaryFigure1.pdf
- Supplymentarytablesfinal.xlsx
- Supplymentarydata1.xlsx

- Supplymentarydata2.xlsx